Thermodynamics of Peptide Inhibitor Binding to HIV-1 gp41

James L. Cole*,‡ and Victor M. Garsky§

Department of Antiviral Research and Department of Medicinal Chemistry, Merck Research Laboratories, West Point, Pennsylvania 19486

Received January 12, 2001; Revised Manuscript Received March 7, 2001

ABSTRACT: The gp41 subunit of the human immunodeficiency virus type 1 envelope glycoprotein mediates fusion of the cellular and viral membranes. The gp41 ectodomain is a trimer of α-helical hairpins, where N-terminal helices form a parallel three-stranded coiled-coil core and C-terminal helices pack around the core. A deep hydrophobic pocket on the N-terminal core represents an attractive target for antiviral therapeutics. We have employed a soluble derivative of the gp41 core ectodomain and small cyclic disulfide D-peptide inhibitors to define the stoichiometry, affinity, and thermodynamics of ligand binding to this pocket using isothermal titration calorimetry. These inhibitors bind with micromolar affinity to the pocket with the expected stoichiometry of three peptides per gp41 core trimer. There are no cooperative interactions among the three binding sites. Linear eight- or nine-residue D-peptides derived from the pocket-binding domain of the cyclic molecules also bind specifically. A negative heat capacity change is observed and is consistent with burial of hydrophobic surface upon binding. Contrary to expectations for a reaction dominated by the classical hydrophobic effect, peptide binding is enthalpically driven and is opposed by an unfavorable negative entropy change. The calorimetry data support models whereby dominant negative inhibitors bind to a transiently exposed surface on the prefusion intermediate state of gp41 and disrupt subsequent resolution to the fusion-active six-stranded hairpin conformation.

Cellular infection by HIV-1[1] is initiated by binding of the viral envelope glycoprotein to cellular receptors, initiating a cascade of events that eventually lead to fusion of the viral envelope and the cellular membrane and delivery of the viral capsid into the cell (*1*). The envelope glycoprotein is composed of the gp120 extracellular subunit involved in receptor binding and the gp41 transmembrane subunit, which mediates fusion. Binding of gp120 to the CD4 receptor and an appropriate chemokine coreceptor triggers a conformational change in gp41 from an inactive resting state into a fusogenic state. The sequence of gp41 contains an N-terminal fusion peptide, thought to insert into the host cell membrane followed by two heptad-repeat sequences, a transmembrane domain, and a cytoplasmic region. Several crystal structures have been reported for the extracellular core domain of HIV-1 gp41 (*2*−*4*). Both X-ray crystal (*5*, *6*) and NMR (*7*) structures are available for the analogous SIV construct. In all of these structures, a trimer of α-helical hairpins is assembled to form a rod-shaped molecule. The N-terminal helices form a parallel three-stranded coiled coil connected via a short loop region to the C-terminal helices, which pack outside the N-helices. In several fusion models, conversion from the resting state to the fusogenic state occurs via a prefusion intermediate in which the N- and C-helix regions are exposed and the fusion peptide is inserted into the cellular membrane (*3*, *4*, *8*, *9*). Subsequently, the N- and C-helices resolve to form the six-helix bundle observed in the structural studies, resulting in apposition of the cellular and viral membranes, and eventually fusion. This mechanism is analogous to that suggested for influenza and several other enveloped viruses and for cellular SNARE proteins which mediate vesicle fusion (*10*).

There is intense interest in the development of alternative AIDS therapeutic agents, and gp41 represents an attractive antiviral target. Linear peptides derived from portions of the N- and C-helices of gp41 are effective inhibitors of viral infection, with the C-helix peptides being considerably more potent (*11*, *12*). One of the C-helix-derived peptides, T-20 (previously called DP-178), suppresses HIV-1 replication in humans (*13*). The C-peptides are believed to act in a dominant-negative manner on gp41 by binding to the N-terminal coiled coil in the susceptible prefusion intermediate, and thus preventing gp41 from resolving into the final hairpin structure. Consistent with this model, T-20 binds to gp41 only after interaction of the viral envelope with cellular receptors (*9*). Alternatively, Caffrey et al. have observed that the gp41 ectodomain from SIV undergoes a reversible monomer−trimer equilibrium, and they suggest that the monomeric state is the primary target for inhibition by exogenous peptides (*7*, *14*).

Three hydrophobic grooves run along the surface of the N-helix trimer and make extensive interactions with side chains from residues in the **a** and **d** positions of the C-helices. Near the C-terminal end of the coiled coil, this groove forms a 400 Å^3 pocket, which has been proposed as a good binding

* To whom correspondence should be addressed: Merck Research Laboratories, WP16-201, West Point, PA 19486. Telephone: (215) 652-5876. Fax: (215) 652-0994. E-mail: jim_cole@merck.com.

‡ Department of Antiviral Research.

§ Department of Medicinal Chemistry.

[1] Abbreviations: ACES, *N*-(carbamoylmethyl)-2-aminoethanesulfonic acid; CD, circular dichroism; HIV-1, human immunodeficiency virus type 1; HPLC, high-pressure liquid chromatography; ITC, isothermal titration calorimetry; MES, 2-(*N*-morpholino)ethanesulfonic acid; SIV, simian immunodeficiency virus.

10.1021/bi010085w CCC: $20.00
Published on Web 04/18/2001

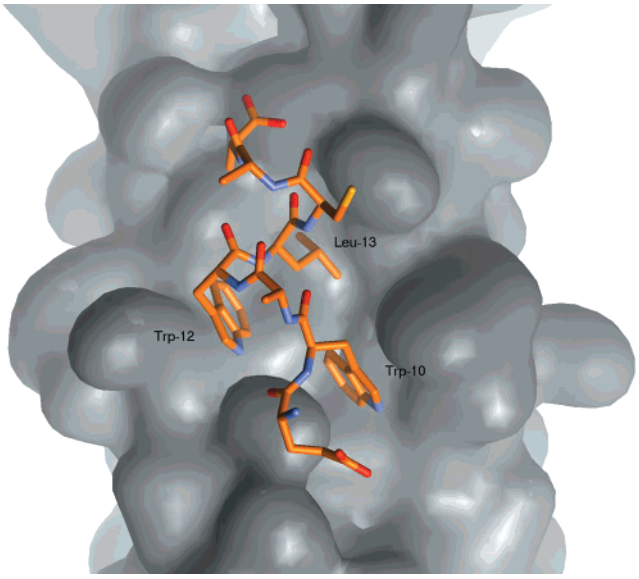

FIGURE 1: X-ray crystal structure of a D-peptide bound to the gp41 pocket. The 1.5 Å structure of the D10-p1−IQN17 complex [PDB entry 1CZQ (*17*)] displayed with the gp41 pocket represented as a molecular surface and D10-p1 in stick format. Only D10-p1 residues from Gly-9 to Ala-16 are shown.

site for a small molecule gp41 inhibitor (*3*, *15*). Three hydrophobic side chains from the C-helix (Trp-628, Trp-631, and Ile-635) project deeply into this cavity and are important for the stability of the six-helix bundle and for viral fusion (*15*). Although the T-20 peptide does not extend into this pocket, a variant of T-20 which encompasses this region is more effective against primary isolates and the inhibition is less susceptible to the development of resistance mutations (*16*).

Two groups have screened for inhibitors that specifically target this hydrophobic pocket. Eckert et al. screened phage libraries for binding to a soluble gp41 N-terminal coiled-coil construct and selected a family of cyclic D-peptides which bind within the hydrophobic pocket and inhibit viral fusion (*17*). The crystal structure of the peptide−gp41 complex (Figure 1) reveals that three peptide residues (Trp, Trp, and Leu) are deeply buried in the pocket, although their conformation differs from that of the native C-helix residues (Trp, Trp, and Ile). Ferrer et al. screened hybrid molecules composed of a conserved C-peptide fragment fused to a three-position combinatorial chemical library (*18*). The peptide serves to target the chemical library to the hydrophobic cavity. A hybrid ligand was identified in which the non-natural portion conferred about a 20-fold increase in potency relative to the peptide alone. In the crystal structure of a complex of the hybrid ligand with the gp41 core, the non-natural portion binds at the pocket and contacts several of the residues involved in binding of the native C-helix (*19*).

Several in vitro assays have been used to characterize binding of C-peptides and inhibitors to the gp41 N-terminal coiled coil: thermal stability (*15*, *20*), in vitro refolding (*18*), colorimetric (*18*), immuno (*21*), and NMR line shift (*17*). Despite the wealth of structural data and biological inhibition studies, in vitro mechanistic studies of inhibitor binding to gp41 have been limited, due to the tendency of the hydrophobic N-peptides to aggregate (*20*). The solubility of the N-helix is enhanced by fusing it in appropriate register to a trimeric, hydrophilic coiled coil derived from GCN4 (*17*, *18*). We have also found that the solubility and homogeneity of at least one of these constructs, IQN17, are improved at lower pH (vide infra).

In the study presented here, isothermal titration calorimetry (ITC) was used to define the thermodynamics of inhibitor binding to the hydrophobic pocket. ITC is a direct method for characterizing the stoichiometry, affinity, and enthalpy of binding reactions in solution (*22*−*24*). We interpret the thermodynamic data in the context of the crystal structure of the gp41−D-peptide complex and antiviral inhibition data. The calorimetry data support models whereby dominant negative inhibitors bind to a transiently exposed surface on the prefusion intermediate state of gp41 and disrupt subsequent resolution to the fusion-active six-stranded hairpin conformation.

MATERIALS AND METHODS

Unless otherwise indicated, measurements were performed in buffer containing 100 mM NaCl, 50 mM MES, and 1 mM EDTA (pH 6.00). The peptides IQN17, D10-p4-2K, D10-p5-2K, C8, and C11 were made by solid-phase synthesis, using a double-coupling protocol for the introduction of all amino acids on a model 430A ABI automated peptide synthesizer. Deprotection and removal of the peptides from the resin support were effected by treatment with liquid HF. The peptides were purified by HPLC on a reverse-phase C18 silica column (25 cm × 6.4 cm) with an acetonitrile/H_2O gradient containing 0.1% trifluoroacetic acid. Homogeneity was demonstrated by analytical HPLC, and the identity was confirmed by amino acid and mass spectral analysis. All other peptides were synthesized by Midwest Biotech, Inc. IQN17 was dissolved in deionized water and dialyzed overnight against buffer, and peptide ligands were dissolved in the dialysate. The IQN17 concentration was determined spectrophotometrically using a molar extinction coefficient ϵ_{280} of 8740 M^{-1} cm^{-1} determined by quantitative amino acid analysis. For D10-p4-2K, ϵ_{280} was measured to be 11 400 M^{-1} cm^{-1}.

Isothermal titration calorimetry was performed using a MicroCal VP ITC calorimeter. Baseline correction, peak integration, and dilution corrections were performed using the ORIGIN analysis software supplied with the instrument. The integrated heat data were analyzed using the IGOR Pro software package (Wavemetrics). The expression for the heat released per injection, $\Delta Q(i)$, is given by

$$\Delta Q(i) = Q(i) + \frac{dV_i}{2V_0}[Q(i) + Q(i-1)] - Q(i-1) \quad (1)$$

where $Q(i)$ is total heat content, dV_i is the volume injected at the ith injection, and V_0 is the cell volume. For fitting data to a model with a single class of identical binding sites, the expression for the total heat is

$$Q = \frac{NM_t\Delta HV_0}{2}\left[1 + \frac{L_t}{NM_t} + \frac{1}{NKM_t} - \sqrt{\left(1 + \frac{L_t}{NM_t} + \frac{1}{NKM_t}\right)^2 - \frac{4L_t}{NM_t}}\right] \quad (2)$$

where N is the stoichiometry, M_t is the total concentration of IQN17, and L_t is the total ligand concentration. The

Table 1: Peptide Sequences

Name	Sequence[a]	Modification
IQN17	Acetyl-RMKQIEDKIEEIESKQKKIENEIARIKKLLQLTVWGIKQLQARIL-amide	
D10-p1-2K	Acetyl-KKGACEARHRE**WA**W**L**CAA-amide	D-amino acid
D5-p1	Acetyl-E**WA**W**L**SAA-amide	D-amino acid
D5-p1-1K	Acetyl-KE**WA**W**L**SAA-amide	D-amino acid
L5-p1-1K	Acetyl-KE**WA**W**L**SAA-amide	
D10-p4-2K	Acetyl-KKGACDLKAKE**W**F**WL**CAA-amide	D-amino acid
D10-p4S-2K	Acetyl-KKGASDLKAKE**W**F**WL**SAA-amide	D-amino acid
D10-p5-2K	Acetyl-KKGACELLGWE**WA**W**L**CAA-amide	D-amino acid
C8	Acetyl-**W**ME**W**DRE**I**-amide	
C11	Acetyl-**W**ME**W**DRE**I**NNY-amide	

[a] The ligand peptide sequences are aligned at the N-terminal tryptophan residue which binds to the hydrophobic pocket. The three pocket binding residues (WWL or WWI) are indicated in boldface.

experimental data were fit to eq 2 using the Marquardt−Levenberg nonlinear least-squares fitting algorithm.

To test for cooperative binding, data were fit to a more general model where the affinity and ΔH for the three binding sites are allowed to differ. The corresponding expression for the total heat is

$$Q = M_t V_0[F_1\Delta H_1 + F_2(\Delta H_1 + \Delta H_2) + F_3(\Delta H_1 + \Delta H_2 + \Delta H_3)] \quad (3)$$

where F_i is the fraction of IQN17 having i bound ligands, which is given by

$$F_0 = \frac{1}{P};\ F_1 = \frac{K_1[\mathrm{L}]}{P};\ F_2 = \frac{K_1K_2[\mathrm{L}]^2}{P};\ F_3 = \frac{K_1K_2K_3[\mathrm{L}]^3}{P} \quad (4)$$

and

$$P = 1 + K_1[\mathrm{L}] + K_1K_2[\mathrm{L}]^2 + K_1K_2K_3[\mathrm{L}]^3 \quad (5)$$

The total and free ligand concentrations are related by

$$L_t = [\mathrm{L}] + M_t\sum_{i=1}^{N} iF_i \quad (6)$$

For given set of equilibrium constants, eqs 4−6 were solved for [L] by bisection and the heat content calculated from eq 3 was fit to the experimental data. For noninteracting, identical sites, the macroscopic equilibrium constants are given by $K_1 = 3k$, $K_2 = k$, and $K_3 = k/3$, where k is the microscopic equilibrium constant. Cooperativity was tested by including a cooperativity parameter ω such that $K_1 = 3k$, $K_2 = \omega k$, and $K_3 = \omega k/3$.

Analytical ultracentrifugation was performed with a Beckman XL-I centrifuge and an An-60Ti rotor at a temperature of 20 °C using absorption optics at 280 nm. Velocity experiments were performed using a 400 μL sample volume in two-sector charcoal-Epon cells at 55 000 rpm, and equilibrium experiments were performed using a 110 μL sample volume in six-sector charcoal-Epon cells at 32 000 and 38 000 rpm. Velocity data were fit to numerical solutions of the Lamm equation with SEDFIT (*25*, *26*). Equilibrium data were analyzed using the Marquardt−Levenberg least-squares algorithm using macros written within the IGOR Pro (Wavemetrics) package. Hydrodynamic modeling and partial specific volume calculations were performed using SEDNTERP (*27*).

Circular dichroism spectra were recorded at 25 °C using 1 mm path length cells with a Jasco model J-810 spectrometer.

RESULTS

Analytical Ultracentrifugation. Sedimentation equilibrium and velocity measurements were performed to assess the association state and homogeneity of IQN17 and the peptide ligands under conditions used for the ITC studies. The sequences are given in Table 1. Initial studies indicated that IQN17 precipitates readily in phosphate buffer at pH 7.4 at peptide concentrations of >0.2 mg/mL. In addition, sedimentation equilibrium measurements in this buffer give a molecular mass of 21 500 Da. The theoretical molecular mass for a trimer of IQN17 is 16 420 Da, indicating the presence of higher multimers, possibly tetramers. In addition, sedimentation velocity indicates heterogeneity in this buffer system (data not shown). In contrast, at pH 6 in MES buffer, IQN17 is soluble to a concentration of >0.5 mg/mL. Global analysis of sedimentation equilibrium data obtained in the buffer at 32 000 and 38 000 rpm gives a molecular mass of 16 650 ± 260 Da, in close agreement with that expected for a trimer. There was no evidence of trimer dissociation. The weight-average molecular mass of the complex of the cyclic D-peptide D10-p4-2K and IQN17 is greater than that of IQN17 alone, suggesting that the trimer remains associated upon ligand binding.

The hydrodynamic properties of IQN17 were characterized by sedimentation velocity analysis (Figure 2A). The sedimentation profiles fit well to a single-species model with a sedimentation coefficient s of 1.48 S and a molecular mass of 16 015 ± 640 Da. Hydrodynamic modeling of the frictional properties of the trimer as a cylinder gives dimensions of 65 Å long × 25 Å wide, in good agreement with the crystal structure (~70 Å long × ~30 Å wide). To asses the homogeneity of the preparation, the velocity data were also fit using a continuous sedimentation coefficient distribution model, and only a single, sharp peak is observed (Figure 2B). Thus, in the pH 6 MES buffer, IQN17 exists as a soluble, homogeneous, and stable trimer.

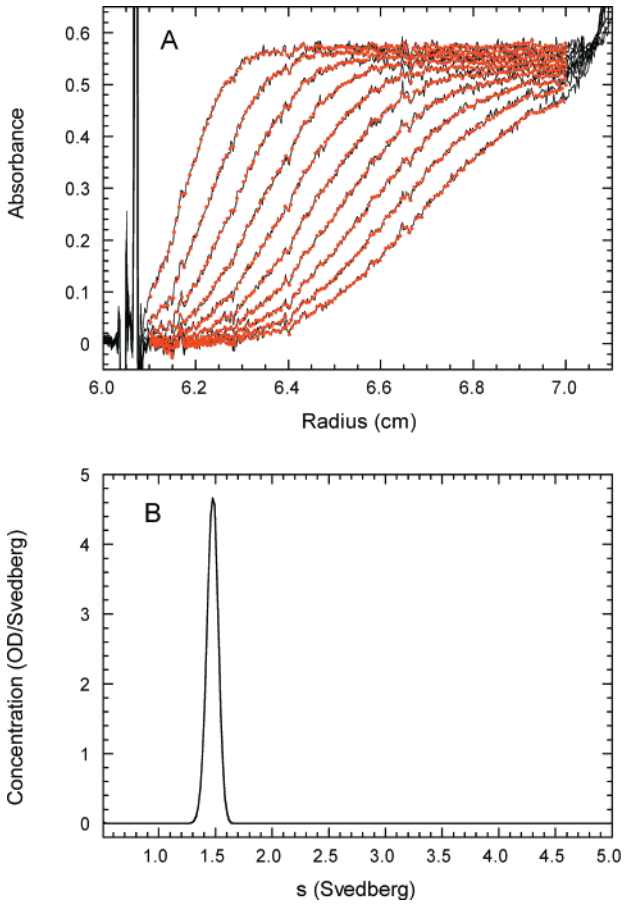

FIGURE 2: (A) Sedimentation velocity of IQN17. Solid black lines show experimental data, and red circles show fitted data. Sample concentration, 0.36 mg/mL (65 μM monomer); wavelength, 280 nm; rotor speed, 55 000 rpm; scan interval, 10 min. For clarity, only every third scan is shown. Data were fit using SEDFIT to give the following best-fit parameters: $s = 1.48$ S and $M = 16\,015 \pm 640$ Da. (B) Continuous sedimentation coefficient distribution of IQN17. The data depicted in panel A were fit to a continuous sedimentation coefficient distribution function using a frictional ratio f/f_0 of 1.30.

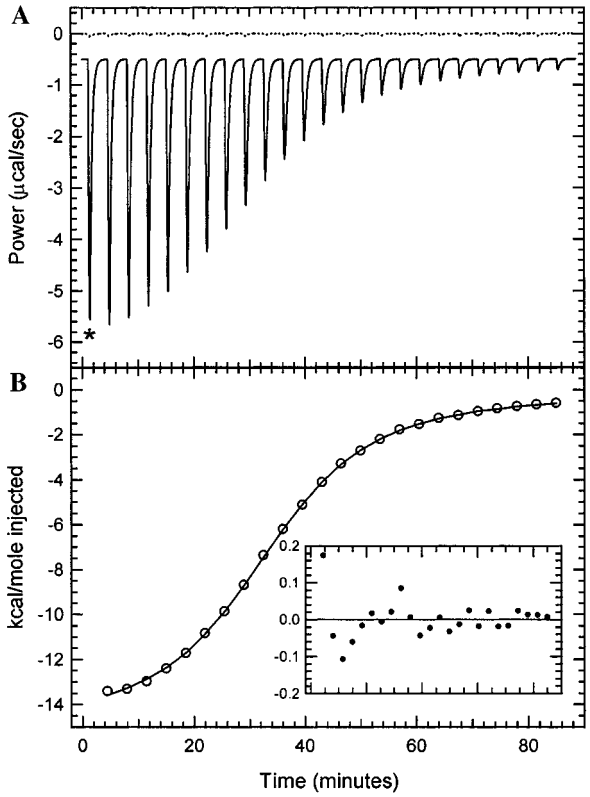

FIGURE 3: Calorimetric titration of D10-p4-2K binding to IQN17. A total of 25 injections (10 μL) were performed at 25 °C. (A) Raw power traces. The solid line is a titration of 1.35 mM D10-p4-2K into 85 μM IQN17, and the dashed line is a control titration of ligand into pure buffer. (B) Integrated areas normalized to the moles of ligand per injection. The open circles are the data, and the solid line is the least-squares fit to the data. The inset is a plot of the residuals. Best-fit parameters are given in Table 2.

With the exception of D10-p5-2K, all of the peptide ligands examined were found to be soluble up to at least 3 mg/mL (1.4 mM). The solubility of D10-p5-2K was limited to ~0.3 mg/mL. In sedimentation measurements of D10-p4-2K, only the monomeric peptide was detected (data not shown).

ITC of Cyclic Peptide Binding to IQN17. Figure 3A shows a calorimetric titration of IQN17 with one of the cyclic D-peptides, D10-p4-2K. Each ligand injection gives rise to a negative (exothermic) heat of reaction, and the peaks become successively smaller as the binding sites on IQN17 become saturated with ligand. In contrast, for systems exhibiting substantial positive cooperativity, the peak amplitudes increase and then decrease during the course of a calorimetric titration (*28*). Also shown in Figure 3A is a titration of D10-p4-2K into buffer to determine the heat of dilution. In this case, the magnitudes of the peaks are significantly smaller, indicating that the heats in the peptide−IQN17 interaction contain little background contribution from ligand dilution effects. Figure 3B shows a fit of the integrated data from Figure 3A to a simple model of identical, noninteracting binding sites; the inset shows the residuals, and the best-fit parameters are listed in Table 2. The data fit this simple model well, and the stoichiometry determined from the fit is close to three peptides per IQN17 core trimer, suggesting that the three hydrophobic cavities displayed on IQN17 behave as independent and identical binding sites under these conditions. However, simulations indicate that weak positive cooperativity would be difficult to observe under the conditions used to produce the data depicted in Figure 3A, where the product of the concentration of IQN17 and the binding constant is ~10. Cooperativity becomes more detectable at lower IQN17 concentrations. Table 2 shows the analysis of a titration of IQN17 with D10-p4-2K performed at a much lower IQN17 concentration (17 μM). Again, the data fit a simple independent site model well, with best-fit parameters similar to those obtained at the higher concentration of IQN17. There is no substantial improvement in the quality of the fit in which the cooperativity coefficient (ω) is allowed to vary, and the best-fit value is not significantly different from 1 (no cooperativity). Furthermore, fixing ω at values of 1.5 and 2.0 results in significantly worse fits, giving rise to 35 and 90% increases in the rmsd from the best-fit value, respectively.

To interpret the observed heat of reaction in an ITC binding experiment as a true binding enthalpy, it is necessary to correct for linked reactions, in particular, buffer enthalpy contributions due to linked protonation changes. The intrinsic binding enthalpy change is obtained by performing parallel experiments in buffers with different ionization enthalpies (*29*). The IQN17 D10-p4-2K interaction was characterized

Table 2: Thermodynamic Binding Parameters

ligand	conc (μM)	[IQN17] (μM)	T (°C)	N	K (M^{-1})	K_d (μM)	$\Delta G°$ (kcal/mol)	ω[a]	$\Delta H°$ (kcal/mol)	$\Delta S°$ (cal deg^{-1} mol^{-1})	rms[b]
D10-p4-2K	234	18	25	2.8	$(2.29 \pm 0.36) \times 10^5$	4.37	-7.28 ± 0.09	1.00 (F)[c]	-14.50 ± 0.88	-24.2 ± 3.0	0.247
D10-p4-2K	234	18	25	2.8 (F)	$(2.14 \pm 0.54) \times 10^5$	4.67	-7.24 ± 0.15	1.04 ± 0.09	-14.76 ± 1.23	-25.2 ± 4.2	0.247
D10-p4-2K	1350	85	25	3.5	$(1.22 \pm 0.03) \times 10^5$	8.20	-6.91 ± 0.02	1.00 (F)	-14.92 ± 0.10	-26.9 ± 0.3	0.690
D10-p4-2K	1350	85	15	3.3	$(2.09 \pm 0.05) \times 10^5$	4.78	-6.99 ± 0.01	1.00 (F)	-13.41 ± 0.06	-22.3 ± 0.2	0.586
D10-p4-2K	1350	85	35	3.4	$(6.18 \pm 0.11) \times 10^4$	16.2	-6.73 ± 0.01	1.00 (F)	-16.76 ± 0.09	-21.8 ± 0.3	0.374
D10-p4-2K[d]	407	40	25	3.3	$(1.57 \pm 0.08) \times 10^5$	6.36	-7.06 ± 0.03	1.00 (F)	-14.60 ± 0.23	-25.3 ± 0.8	0.27
D10-p4S-2K	1420	88	25	3 (F)	$(4.06 \pm 0.34) \times 10^3$	246	-4.90 ± 0.05	1.00 (F)	-11.87 ± 0.90	-23.4 ± 3.05	0.310
D10-p5-2K	140	18	25	3.4	$(8.53 \pm 2.15) \times 10^5$	1.17	-8.06 ± 0.15	1.00 (F)	-9.77 ± 0.11	-5.73 ± 0.6	0.241
D10-p1-2K	859	58	25	4.4	$(1.15 \pm 0.03) \times 10^5$	8.68	-6.88 ± 0.01	1.00 (F)	-16.55 ± 0.08	-32.5 ± 0.3	0.301
D5-p1	917	100	25	3 (F)	$(9.50 \pm 2.67) \times 10^3$	106	-5.40 ± 0.17	1.00 (F)	-12.45 ± 2.45	-23.7 ± 8.3	0.294
D5-p1-1K	1110	88	25	2.8	$(1.54 \pm 0.09) \times 10^4$	65.1	-5.69 ± 0.04	1.00 (F)	-11.72 ± 0.48	-20.2 ± 1.6	0.190
L5-p1-1K	1670	88	25		no binding detected						
C8	1090	35	25		no binding detected						
C11	1210	85	25		no binding detected						

[a] Cooperativity parameter. [b] Root-mean-square deviation of the fit (microcalories). [c] F indicates the parameter was fixed during the fit. [d] Titration performed in 50 mM ACES, 100 mM NaCl, and 1 mM EDTA (pH 6.0).

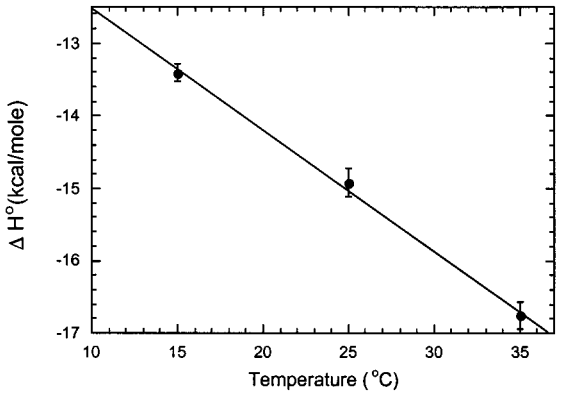

FIGURE 4: Temperature dependence of the enthalpy change for binding of D10-p4-2K to IQN17. The slope of the best-fit line gives a heat capacity change, $\Delta C_p°$, of -168 kcal/mol.

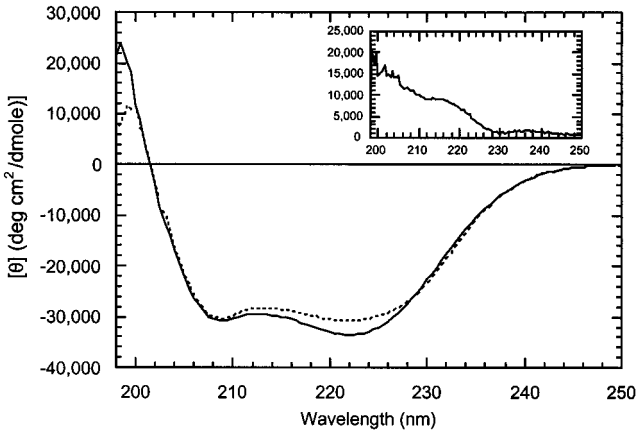

FIGURE 5: Effect of ligand binding on the circular dichroism spectrum of IQN17: (−) IQN17 alone and (- - -) IQN17 with stoichiometric D10-p4-2K. Spectra were recorded at an IQN17 concentration of 50 μM at 25 °C in 1 mm path length cells. The inset shows the circular dichroism spectrum of D10-p4-2K alone. The intensity at 222 nm for pure α-helix is -36000 deg cm^{-2} $dmol^{-1}$.

in ACES buffer, and the apparent enthalpy change was measured to be -14.60 kcal/mol, 0.32 kcal/mol less negative than in MES buffer (Table 2). The ionization enthalpies for ACES and MES buffer are 7.47 and 3.73 kcal/mol, respectively (*29*), so that each proton linked to the binding reaction will result in a difference of $7.47 - 3.73 = 3.74$ kcal/mol in the heat of reaction in the two buffers. Therefore, at pH 6 the small shift of 0.32 kcal/mol in the observed heat indicates that less than 0.1 proton is taken up per peptide bound. It is not possible to evaluate peptide binding at higher pH values due to the tendency of IQN17 to aggregate. The observed heat of reaction can be equated with the intrinsic enthalpy change, and the relationship $\Delta G° = \Delta H° - T\Delta S°$ can be used to obtain the entropy change: $\Delta S° = -26.9 \pm 0.7$ cal deg^{-1} mol^{-1} at 25 °C. Thus, binding of D10-p4-2K to the gp41 hydrophobic pocket is driven by a large negative enthalpy and is opposed by a large negative entropic contribution.

The heat capacity change, $\Delta C_p°$, is a fundamental thermodynamic parameter, which can be directly obtained from the temperature dependence of the binding enthalpy according to the equation $\Delta C_p° = (\partial \Delta H/\partial T)_P$. The temperature dependence of the binding of D10-p4-2K to IQN17 was characterized over a temperature range of 15−35 °C (Table 2), and Figure 4 is a plot of $\Delta H°$ versus temperature. The enthalpy change varies linearly with temperature over this range, and the slope of the plot gives the heat capacity change ($\Delta C_p° = -168$ cal deg^{-1} mol^{-1}). Negative heat capacity changes are typically observed in protein−protein interactions and are associated with the burial of solvent-accessible hydrophobic surface area (*30*). Empirical relationships have been developed to predict $\Delta C_p°$ based on the amount of apolar and polar solvent-accessible surface area buried upon binding. The parameters reported by Murphy and Freire (*31*) and Spolar and Record (*32*) predict $\Delta C_p°$ values of -307 and -226 cal deg^{-1} mol^{-1}, respectively. Both predictions are somewhat larger than the experimentally determined value of -168 cal deg^{-1} mol^{-1}, but qualitatively agree. Conformational changes linked to binding can also contribute to $\Delta C_p°$. CD spectroscopy was used to test for changes in secondary structure linked to ligand binding. Figure 5 shows the far-UV CD spectrum of IQN17 alone and the spectrum of the complex of IQN17 with D10-p4-2K. As previously reported (*17*), the CD intensity at 222 nm for IQN17 indicates that it is fully α-helical in solution. Binding of D10-p4-2K results in a decrease in the intensity at 222 nm, and the amplitude change is consistent with folding of approximately five residues of the ligand into a left-handed α-helix (the CD contribution of left-handed α-helix is positive, the opposite of that of the conventional right-handed helix). The

inset of Figure 5 shows the CD spectrum of the ligand alone. This spectrum is characteristic of predominant random coil. In the D10-p1−IQN17 complex, the ligand segments from Ala-2 to Ala-5 and from Ala-11 to Ala-16 are in a left-handed α-helical conformation (*17*). Thus, the experimental CD change is somewhat smaller than expected from the crystal structure, indicating that these residues are not fully folded in solution or that IQN17 is slightly perturbed upon ligand binding. In either case, CD indicates that no substantial changes in the secondary structure IQN17 occur upon binding of cyclic D-peptide.

D10-p4-2K is one member of a family of eight cyclic D-peptides in which the residues directly contacting IQN17 are completely conserved (*17*). To confirm that D10-p4-2K is representative of this series, two other cyclic D-peptides, D10-p1-2K and D10-p5-2K, were characterized by ITC (Table 2). Differences in affinity for IQN17 are observed: binding of D10-p1-2K is slightly weaker and D10-p5-2K ∼3-fold stronger than D10-p4-2K. In vivo, the rank order for inhibition of viral infectivity is different: D10-p1-2K is ∼2-fold *more* potent and D10-p5-2K 15−20-fold more potent (*17*). Despite these slight differences in relative potencies, the in vitro dissociation constants are always lower than the in vivo IC_{50} values. In all three cases, $\Delta H°$ and $\Delta S°$ are both negative; however, there are interesting quantitative differences. Relative to D10-p4-2K, there is a large decrease in unfavorable entropy for D10-p5-2K, which is accompanied by a parallel decrease in favorable enthalpy. Similarly, the enthalpy and entropy increase in parallel for D10-p1-2K. This linked variation in $\Delta H°$ and $\Delta S°$ is characteristic of enthalpy−entropy compensation.

ITC of Linear Peptide Binding to IQN17. Most of the 18 residues comprising the cyclic D-peptide ligand series do not interact with the hydrophobic pocket. Six ligand residues directly bind to the pocket, and most of the interaction surface is derived from the side chains of Trp-10, Trp-12, Leu-13, and Ala-16 (Figure 1) (*17*). Two peptides, D5-p1 and D5-p1-1K, were synthesized so that they contained the EWAWLSAA sequence which encompasses these core binding residues, with the consensus Cys residue changed to Ser to avoid intermolecular disulfide bond formation. These short, linear peptides bind to IQN17 with K_d values of 106 and 65 μM, respectively (Table 2). For D5-p1-1K, the stoichiometry is close to the expected three molecules per IQN17 trimer; for D5-p1, the affinity is too low to treat the stoichiometry as an adjustable fit parameter. Like binding of the parent cyclic disulfide D-peptides, binding of the short linear D-peptides is enthalpically driven, and is opposed by a negative entropy change. To confirm the specificity of these relatively weak interactions, a control peptide, L5-p1-1K, was synthesized with the same sequence as D5-p1-1K but composed of L-amino acids. As assessed by ITC, there is no saturable binding of L5-p1-1K to IQN17 (Table 2).

The decrease in the affinity of the linear D-peptides relative to the parent cyclic molecules is likely due to the loss of the conformational rigidity provided by the disulfide linkage. The role of this disulfide linkage was examined directly using D10-p4S-2K, an analogue of D10-p4-2K in which the Cys residues are replaced with Ser residues. This ligand binds ∼50-fold more weakly than the disulfide-linked peptide, with most of the loss in affinity occurring due to a decrease in binding enthalpy. Interestingly, this peptide binds even weaker than the linear sequences D-5-P1 and D-5-p1-1K. Thus, the loss of affinity of the short linear D-peptides relative to the larger cyclic molecules is due in large part to the loss of conformational rigidity imposed by the disulfide linkage. Consistent with this finding, in the original phage library, the flanking region was composed of either Cys or Ser residues, but the sequences retrieved from the selection experiment always contained Cys (*17*). In addition, analogues of the cyclic D-peptides in which the Cys residues are replaced with Ala lack inhibitory activity in antiviral assays (*17*).

In the crystal structure of the gp41 ectodomain, three C-helix residues (Trp-628, Trp-631, and Ile-635) are deeply buried in the hydrophobic cavity. Two peptides, C8 and C11, which encompass these residues, were characterized for binding to the hydrophobic pocket in IQN17. In contrast to the linear D-peptides described above, for both C8 and C11 the only ITC signal corresponds to the heat of dilution, indicating that binding is much weaker or does not occur. These sequences have also have been found to lack antiviral activity (*15*). Due to the limited size of the gp41 coiled coil contained within the IQN17 construct, it is not possible to extend the sequence of C11 to determine the minimal fragment of C-helix that is capable of binding specifically to the N-helix coiled coil.

DISCUSSION

Although potent molecules, such as T-20, have been available for some time, mechanistic studies of HIV entry inhibitors targeted to gp41 have been hampered by a lack of suitable reagents and methodologies. The recently characterized soluble derivatives of the gp41 N-helix core and specific ligands (*17*, *18*) constitute a valuable model system for probing the binding equilibria that underlie HIV inhibition using direct biophysical measurements. In the study presented here, we have employed ITC to define stoichiometry, affinity, and thermodynamics governing interaction of the cyclic D-peptides and related subdomains with the gp41 hydrophobic pocket. The qualitative features governing binding of each of the D-peptides that were examined are quite similar. The inhibitors bind with a stoichiometry of approximately three ligands per IQN17 core trimer with equilibrium dissociation constants in the micromolar range. Each of the binding sites behaves independently with no evidence of cooperative interactions. Binding is driven by a favorable negative enthalpy change and is opposed by a negative entropy change.

The ITC data provide support for previous models whereby dominant negative gp41 inhibitors bind to surfaces transiently exposed on the prefusion intermediate and disrupt subsequent resolution to the fusion-active six-stranded hairpin structure (*3*, *4*, *8*, *9*). The dissociation constants for cyclic D-peptide binding to IQN17 are 3−10-fold lower than the corresponding IC_{50} values reported for HIV inhibition. Although differences in experimental conditions make it difficult to directly compare in vitro ITC results with the biological data, it is noteworthy that the affinity of the D-peptides for IQN17 is comparable to their HIV inhibitory activity. Competition between the endogenous C-helix and the exogenous peptide inhibitors for binding to the hydrophobic pocket in the prefusion intermediate would tend to increase the IC_{50} for

inhibitor binding relative to the equilibrium ligand dissociation constant. The similarity of these values suggests that competition is not significant. This model is supported by observations that the prefusion intermediate is formed rapidly but is stable for several minutes (*33*, *34*), during which time the C-helix is somehow prevented from binding to the N-helix core. The present data do not support an alternative model in which the primary target for the inhibitory peptides is a monomeric state of gp41 (*7*, *14*), since we find that IQN17 remains as a stable trimer in the absence or presence of bound ligand.

In the cyclic D-peptides, most of the interaction surface is contributed by residues Trp-10, Trp-12, Leu-13, and Ala-16 (Figure 1), and short, linear peptides containing this region bind to IQN17. Although the affinity of the linear peptides is lower than that of the original cyclic molecules, the binding mode is relevant because (1) the stoichiometries, where measured, are close to the expected (3:1), (2) binding is stereospecific, and (3) the thermodynamic signatures for the linear and cyclic peptides are similar (large negative enthalpy and negative entropy). Nonetheless, the linear peptides do not exhibit antiviral activity (M. Miller, unpublished data), presumably due to the low binding affinity. Weak affinities are also observed for longer linear peptides derived from D10-p4-2K in which the cysteines are replaced with serines (D10-p4S-2K), indicating that a major contribution to the reduced affinity of the octapeptide is associated with the loss of the conformational constraint of the disulfide linkage.

In contrast to the linear D-peptides described above, the analogous linear L-peptides derived from the pocket binding region of the gp41 C-helix do not interact with IQN17 in the ITC experiments, suggesting that these ligands must bind considerably more weakly. This difference may reflect better complementarity of the un-natural D-peptide than the native C-helix with the pocket region. The cyclic D-peptide buries 458 Å^2 of solvent-accessible surface area of the pocket, but only 297 Å^2 is buried by C-helix binding (*19*). There are also differences in the nature of the intermolecular contacts that may be responsible for the lack of binding of the native peptide. In the D-peptides, the side chain from Trp-10 occupies a plane similar to that of the corresponding C-helix side chain from Trp-628. In contrast, the indole planes from Trp-12 and Trp-631 are orthogonal and the aliphatic side chains from Leu-13 and Ile-635 do not overlay closely. In addition, there is no counterpart to Ala-16 in the C-helix. In the N-helix−C-helix heterotrimer, there is a salt bridge between Asp-632 from the C-helix and the pocket residue Lys-574, and one hydrogen bond forms between the indole nitrogen from Trp-631 in the C-helix and the carbonyl oxygen of Leu-568 from the pocket (2.8 Å). In contrast, there are no intermolecular salt bridges in the D10-P1−IQN17 complex, but two intermolecular hydrogen bonds are formed between the ligand Trp-12 indole and Gln-577 from the pocket (2.9 Å) and the ligand Glu-9 carbonyl oxygen and Gln-577 (3.1 Å). The two hydrogen bonds in the D-peptide−pocket interaction may confer enhanced stability relative to one hydrogen bond and one salt bridge. Alternatively, the difference in binding may reflect an intrinsic difference in the propensities for the two peptides to adopt a helical conformation upon binding.

Although the interface of the cyclic D-peptides and IQN17 is predominantly apolar, the thermodynamics are not typical of an interaction driven by the classical hydrophobic effect. From the crystal structure, the changes in apolar and polar solvent-accessible surface areas are calculated to be −774 and −156 Å^2, respectively. In the classical picture, hydrophobic interactions are entropically driven due to removal of ordered solvent molecules from apolar binding interfaces, and are weakly enthalpically unfavorable due to enhanced hydrogen binding among interfacial waters. More recently, it has been shown that the sign of both the enthalpy and entropy of hydrophobic hydration depends on the shape and curvature of the interface (*35*). In contrast to the expected positive $\Delta S°$ and positive $\Delta H°$ for the classical hydrophobic interaction, for all of the D-peptides both parameters are negative. The unfavorable entropy term can be ascribed to ligand configurational effects. Since the cyclic peptides are mostly unstructured in free solution, there is a large configurational entropy penalty associated with folding of the ligand upon binding. Average configurational entropy changes for folding of unconstrained peptides are reported to be in the range of −4 to −5 cal deg^{-1} mol^{-1} per residue (*31*, *32*), giving a configurational contribution to the entropy change of −70 to −90 cal deg^{-1} mol^{-1} for binding of an 18-residue peptide. Thus, without consideration of contributions from the hydrophobic effect or potential reduction of the internal entropy of IQN17 upon binding ligand, the net negative entropy change can easily be ascribed to reduction in the ligand configurational degrees of freedom.

In contrast to the entropy, the interactions responsible for the −9 to −16 kcal/mol favorable enthalpy change are not obvious. A combination of inter- and intramolecular hydrogen bonds may give rise to significant enthalpic stabilization. Two intermolecular hydrogen bonds form between the ligand and IQN17. Formation of a neutral hydrogen bond in water usually contributes about −2 to −3 kcal/mol to the enthalpy of protein−ligand complexation (*36*, *37*). The bound ligand contains two segments of left-handed α-helix with three or four intramolecular hydrogen bonds. The enthalpic contribution to α-helix formation is about 1 kcal/mol per residue (*38*). Thus, an enthalpy contribution from hydrogen bonding of −7 to −10 kcal/mol is expected. Alternatively, the negative enthalpy change may be ascribed to a nonclassical hydrophobic interaction (*35*), as recently observed in several biological systems (*39*, and references therein). Finally, subtle structural rearrangements outside of the interface may contribute significantly to the binding energetics. In biological systems, the origin of binding energy may not be evident at the binding interface; instead, it may reflect an overall "tightening" of the internal structure of the macromolecule (*40*).

It has been suggested that a large negative heat capacity change is a more reliable signature for hydrophobic interactions than $\Delta H°$ or $\Delta S°$ (*30*), and most protein−protein and protein−peptide interactions are associated with a large negative $\Delta C_p°$. In contrast, burial of polar surface area contributes a weakly positive ΔC_p. The heat capacity change for D10-p4-2K binding to IQN17 is negative, albeit weaker than typically observed for protein−peptide interactions (*30*). On the basis of the crystal structure of a D-peptide bound to the gp41 pocket, the empirical relationships reported by Murphy and Freire (*31*) and Spolar and Record (*32*) give $\Delta C_p°$ values of −307 and −226 cal deg^{-1} mol^{-1}, respectively. Both predictions are somewhat larger than the

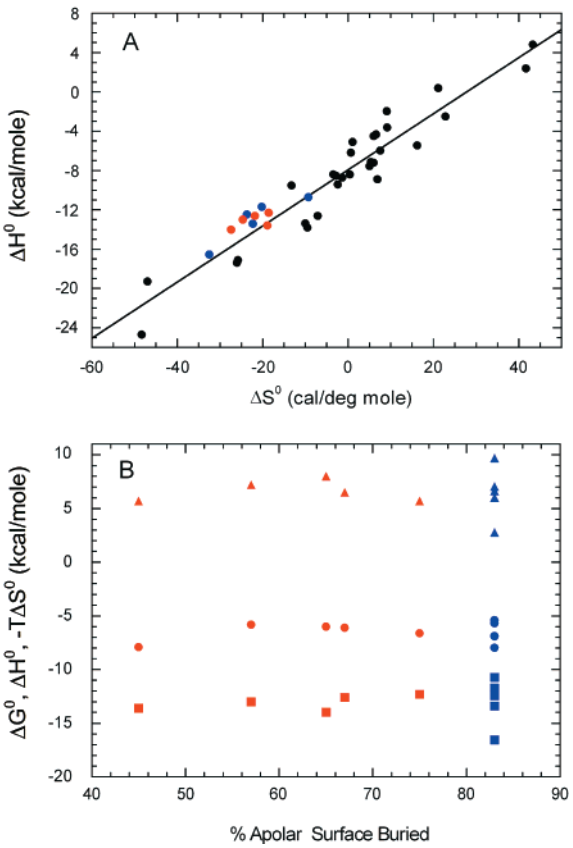

FIGURE 6: Enthalpy−entropy compensation in peptide−protein interactions. (A) Plot of enthalpy−entropy compensation in protein−peptide interactions. Data were obtained from Ye and Wu (*47*), McNemar et al. (*48*), and references cited in the review by Stites (*30*). Black symbols are for protein−peptides interactions, from the literature; blue symbols are for gp41 data from Table 1, and red symbols are for structurally defined protein−peptide interactions with thermodynamics similar to those of gp41: *E. coli* serine receptor/methyltransferase peptide (*49*), TRAF2−OX40 peptide (*47*), TRAF2−CD30 peptide (*47*), streptavidin−strep-tag peptide (*50*), and Fyn SH3 domain−p85 peptide (*51*). (B) Thermodynamic binding parameters as a function of apolar buried surface: (circles) $\Delta G°$, (squares) $\Delta H°$, and (triangles) $-T\Delta S°$. The red symbols correspond to data for the structurally defined protein−peptide systems indicated in red in part A, and the blue symbols represent the gp41 data from this paper. Solvent-accessible surface areas were calculated using published coordinates.

experimentally determined value of −168 cal deg^{-1} mol^{-1}, but there is reasonable agreement.

Enthalpy−entropy compensation is evident in the IQN17−peptide interactions Enthalpy−entropy compensation is the correlation of changes in ΔH and ΔS such that changes in ΔG are minimized and is a general property of weak intermolecular interactions (*41*). In the biological context, compensation has been reported for drug−receptor binding (*42*) and for antigen−antibody interactions (*43*). In the D-peptide series, the ligand with the most negative binding enthalpy (D10-p1-2K) also has the strongest unfavorable entropy change, and conversely, the ligand with the weakest enthalpy (D10-p5−2K) corresponds to the lowest entropy of binding (Table 1), suggesting compensation. Figure 6A shows an entropy−enthalpy correlation plot for a range of interacting protein−peptide systems, including data from this study. As typically observed for enthalpy−entropy compensation, the points show a clear linear trend with a correlation coefficient R of 0.98, and the gp41 data lie along the correlation line. Thus, enthalpy−entropy compensation appears to be a general phenomenon in protein−peptide interactions. The gp41 data lie in the lower left-hand quadrant of the graph with negative enthalpy and entropy changes. High-resolution structural data are available for the points labeled in red that lie within the same region as the IQN17 data. Figure 6B shows the thermodynamic parameters for these protein−peptide systems plotted as a function of the percent apolar surface buried in the binding reaction. The measured values of $\Delta G°$, $\Delta S°$, and $\Delta H°$ are quite similar, but the buried surface area varies from a mixture of polar and apolar to predominantly apolar, with the gp41 the most apolar of the group. The total polar and apolar buried surface area for these systems varies from −775 to −1180 Å^2, and again, there is no obvious correlation with the thermodynamic parameters. The number of hydrogen bonds and salt bridges and the secondary structure of the bound peptides are quite different for these systems (data not shown). These data emphasize the challenges in correlating structure with thermodynamic parameters governing protein−peptide interactions; additional experimental and theoretical approaches will likely be required (*44*).

Although the D-peptides bind weakly to the hydrophobic pocket in gp41, this interaction can potentially be exploited for development of more potent, small molecule HIV entry inhibitors. The phage display method has selected for non-natural peptide ligands that bind to the hydrophobic pocket with substantial negative enthalpy. A challenge for drug design is to maintain the favorable interactions with the pocket while minimizing the unfavorable entropic penalty of binding associated with folding of the ligand upon binding. Entropy−enthalpy compensation will likely oppose attempts to increase affinity by enhancing ligand rigidity. Nonetheless, derivatives of T-20 containing covalent constraints show improved antiviral activity (*8*), and sequence modification of a C-helix peptide for enhancing helicity in solution improves antifusion activity (*45*). Another challenge is to reduce the inhibitor size. In this regard, it is encouraging that peptides as short as eight or nine residues bind specifically to the hydrophobic pocket with substantial negative enthalpy. Nonpeptidic, small molecule ligands show potential for specific interactions with the pocket (*18*, *19*). Alternatively, other regions in the gp41 N-helix core may prove to be suitable for inhibitor design. The clinically efficacious peptide, T-20, binds tightly to a region of the trimeric N-helix outside of the hydrophobic pocket. Unfortunately, extended N-helix peptides encompassing larger regions of the gp41 core aggregate strongly in solution and are not suitable for biophysical studies (*20*). However, an engineered "five-helix" gp41 protein was recently described that may be useful for these studies (*46*). This protein is composed of five of the six helices of the gp41 core and displays an open binding surface for binding of C-peptides but remains monomeric in solution.

ACKNOWLEDGMENT

We thank Michael Miller for useful discussions and for antiviral activity assays, Paul Darke for use of the VP ITC instrument, Joe Joyce for use of the CD spectrometer, Sanjeev Munshi for surface area calculations, and Daria Hazuda for support of this project.

REFERENCES

1. Chan, D. C., and Kim, P. S. (1998) *Cell 93*, 681−684.
2. Tan, K., Liu, J.-H., Wang, J.-H., Shen, S., and Lu, M. (1997) *Proc. Natl. Acad. Sci. U.S.A. 94*, 12303−12308.
3. Chan, D. C., Fass, D., Berger, J. M., and Kim, P. S. (1997) *Cell 89*, 263−273.
4. Weissenhorn, W., Dessen, A., Harrison, S. C., Skehel, J. J., and Wiley, D. C. (1997) *Nature 387*, 426−430.
5. Yang, Z.-N., Mueser, T. C., Kaufman, J., Stahl, S. J., Wingfield, P. T., and Hyde, C. C. (1999) *J. Struct. Biol. 126*, 131−144.
6. Malashkevich, V. N., Chan, D. C., Chutkowski, C. T., and Kim, P. S. (1998) *Proc. Natl. Acad. Sci. U.S.A. 95*, 9134−9139.
7. Caffrey, M., Cai, M., Kaufman, J., Stahl, S. J., Wingfield, P. T., Covell, D. G., Gronenborn, A., and Clore, G. M. (1998) *EMBO J. 17*, 4572−4584.
8. Judice, J. K., Tom, J. Y., Huang, W., Wrin, T., Vennari, J., Petropoulos, C. J., and McDowell, R. S. (1997) *Proc. Natl. Acad. Sci. U.S.A. 94*, 13426−13430.
9. Furuta, R. A., Wild, C. T., Weng, Y., and Weiss, C. D. (1998) *Nat. Struct. Biol. 5*, 276−279.
10. Skehel, J. J., and Wiley, D. C. (1998) *Cell 95*, 871−874.
11. Jiang, S., Lin, K., Strick, N., and Neurath, A. R. (1993) *Nature 365*, 113.
12. Wild, C. T., Oas, T., McDanal, C. B., Bolognesi, D., and Matthews, T. J. (1992) *Proc. Natl. Acad. Sci. U.S.A. 89*, 10537−10541.
13. Kilby, J., Hopkins, S., Venetta, T., DiMassimo, B., Cloud, G., Lee, J., Alldredge, L., Hunter, E., Lambert, D., Bolognesi, D., Matthews, T., Johnson, M., Nowak, M., Shaw, G., and Saag, M. (1998) *Nat. Med. 4*, 1302−1307.
14. Caffrey, M., Kaufman, J., Stahl, S., Wingfield, P., Gronenborn, A. M., and Clore, G. M. (1999) *Protein Sci. 8*, 1904−1907.
15. Chan, D. C., Chutkowski, C. T., and Kim, P. S. (1998) *Proc. Natl. Acad. Sci. U.S.A. 95*, 15613−15617.
16. Rimsky, L. T., Shugars, D. C., and Matthews, T. J. (1998) *J. Virol. 72*, 986−993.
17. Eckert, D. M., Malashkevich, V. N., Hong, L. H., Carr, P. A., and Kim, P. S. (1999) *Cell 99*, 103−115.
18. Ferrer, M., Kapoor, T. M., Strassaier, T., Weissenhorn, W., Skehel, J. J., Oprian, D., Shreiber, S. L., Wiley, D. C., and Harrison, S. C. (1999) *Nat. Struct. Biol. 6*, 953−960.
19. Zhou, G., Ferrer, M., Chopra, R., Kapoor, T. M., Strassaier, T., Weissenhorn, W., Skehel, J. J., Oprian, D., Shreiber, S. L., Harrison, S. C., and Wiley, D. C. (2000) *Bioorg. Med. Chem. 8*, 2219−2228.
20. Lu, M., Blacklow, S. C., and Kim, P. S. (1995) *Nat. Struct. Biol. 2*, 1075−1082.
21. Jiang, S., Lin, K., Zhang, L., and Debnath, A. K. (1999) *J. Virol. Methods 80*, 85−96.
22. Jelesarov, I., and Bosshard, H. R. (1999) *J. Mol. Recognit. 12*, 3−18.
23. Ladbury, J. E., and Chowdry, B. Z. (1996) *Chem. Biol. 3*, 791−801.
24. Fisher, H. F., and Singh, N. (1995) *Methods Enzymol. 259*, 194−221.
25. Schuck, P. (1998) *Biophys. J. 75*, 1503−1512.
26. Schuck, P. (2000) *Biophys. J. 78*, 1606−1619.
27. Laue, T. M., Shah, B. D., Ridgeway, T. M., and Pelletier, S. L. (1992) in *Analytical Ultracentrifugation in Biochemistry and Polymer Science* (Harding, S., Rowe, A., and Horton, J., Eds.) pp 90−125, Royal Society of Chemistry, Cambridge, U.K.
28. Gorshkova, I., Moore, J., McKenney, K., and Schwarz, F. (1995) *J. Biol. Chem. 270*, 21679−21683.
29. Murphy, K. P., Xie, D., Garcia, K. C., Amzel, L. M., and Freire, E. (1993) *Proteins 15*, 113−120.
30. Stites, W. E. (1997) *Chem. Rev. 97*, 1233−1250.
31. Murphy, K. P., and Freire, E. (1992) *Adv. Protein Chem. 43*, 313−361.
32. Spolar, R. S., and Record, M. T. (1994) *Science 263*, 777−784.
33. Jones, P. L., Korte, T., and Blumenthal, R. (1998) *J. Biol. Chem. 273*, 404−409.
34. Munoz-Barroso, I., Durell, S., Sakaguchi, K., Appella, E., and Blumenthal, R. (1998) *J. Cell Biol. 140*, 315−323.
35. Southall, N. T., and Dill, K. A. (2000) *J. Phys. Chem. B 104*, 1326−1331.
36. Haberman, S. M., and Murphy, K. P. (1996) *Protein Sci. 5*, 1229−1239.
37. Davis, A. M., and Teague, S. J. (1999) *Angew. Chem., Int. Ed. 38*, 736−749.
38. Scholtz, J. M., Marqusee, S., Baldwin, R. L., York, E. J., Stewart, J. M., Santoro, M., and Bolen, D. W. (1991) *Proc. Natl. Acad. Sci. U.S.A. 88*, 2854−2858.
39. Ackroyd, P. C., Cleary, J., and Glick, G. D. (2001) *Biochemistry 40*, 2911−2922.
40. Williams, D. H., and Westwell, M. S. (1996) *Chem. Biol. 3*, 695−701.
41. Dunitz, J. D. (1995) *Chem. Biol. 2*, 709−712.
42. Gilli, P., Ferretti, V., Gilli, G., and Borea, P. A. (1994) *J. Phys. Chem. 98*, 1515−1518.
43. Swaminathan, C. P., Nandi, A., Visweswariah, S. S., and Surolia, A. (1999) *J. Biol. Chem. 274*, 31272−31278.
44. Cooper, A. (1999) *Curr. Opin. Chem. Biol. 3*, 557−563.
45. Jin, B.-S., Ryu, J.-R., Ahn, K., and Yu, Y. G. (2000) *AIDS Res. Hum. Retroviruses 16*, 1797−1804.
46. Root, M. J., Kay, M. S., and Kim, P. S. (2001) *Science 291*, 884−888.
47. Ye, H., and Wu, H. (2000) *Proc. Natl. Acad. Sci. U.S.A. 97*, 8961−8966.
48. McNemar, C., Snow, M. E., Windsor, W. T., Prongay, A., Mui, P., Zhang, R., Durkin, J., Le, H. V., and Weber, P. C. (1997) *Biochemistry 36*, 10006−10014.
49. Wu, J., Li, J., Long, D. G., and Weis, R. M. (1996) *Biochemistry 35*, 4984−4993.
50. Schmidt, T. G. M., Koepke, J., Frank, R., and Skerra, A. (1996) *J. Mol. Biol. 255*, 753−766.
51. Renzoni, D. A., Pugh, D. J. R., Siligardi, G., Das, P., Morton, C. J., Rossi, C., Waterfield, M. D., Campbell, I. D., and Ladbury, J. E. (1996) *Biochemistry 35*, 15646−15653.

BI010085W